

# On the ability of spectroscopic SZ effect measurements to determine the temperature structure of galaxy clusters

S. Colafrancesco<sup>1,2</sup> and P. Marchegiani<sup>2,3</sup>

<sup>1</sup> ASI-ASDC c/o ESRIN, Via G. Galilei snc, I-00040 Frascati, Italy Email: Sergio.Colafrancesco@asi.it

<sup>2</sup> INAF - Osservatorio Astronomico di Roma via Frascati 33, I-00040 Monteporzio, Italy. Email: cola@mporzio.astro.it

<sup>3</sup> Dipartimento di Fisica, Università di Roma La Sapienza, P.le A. Moro 2, Roma, Italy Email: marchegiani@mporzio.astro.it

Received / Accepted

## ABSTRACT

**Aims.** We explore in this paper the ability of spatially resolved spectroscopic measurements of the SZ effect (SZE) to determine the temperature profile of galaxy clusters. We derive a general formalism for the thermal SZE in galaxy clusters with a non-uniform temperature profile that can be applied to both cool-core clusters and non-cool core cluster with an isothermal or non-isothermal temperature structure.

**Methods.** We derive an inversion technique through which the electron distribution function can be extracted from spectroscopic SZE observations over a wide frequency range. We study the fitting procedure to extract the cluster temperature from a set of simulated spatially resolved spectroscopic SZE observations in different bands of the spectrum, from 100 to 450 GHz.

**Results.** The results of our analysis for three different cluster prototypes (A2199 with a low-temperature cool core, Perseus with a relatively high-temperature cool core, Ophiuchus with an isothermal temperature distribution) provide both the required precision of the SZE observations and the optimal frequency bands for a determination of the cluster temperature similar or better than that obtainable from X-ray observations. The precision of SZE-derived temperature is also discussed for the outer regions of clusters. We also study the possibility to extract, from our method, the parameters characterizing the non-thermal SZE spectrum of the relativistic plasma contained in the lobes of radio galaxies as well as the spectrum of relativistic electrons co-spatially distributed with the thermal plasma in clusters with non-thermal phenomena.

**Conclusions.** We find that the next generation SZE experiments with spectroscopic capabilities, like those using FTS spectrometers with imaging capabilities, can provide precise temperature distribution measurements over a large range of radial distances for galaxy clusters even out to substantial redshifts.

**Key words.** Cosmology; Galaxies: clusters: theory

## 1. Introduction

Galaxy clusters are the largest gravitationally bound container of diffuse baryons in the universe. These baryons accomodate in the cluster gravitational potential well dominated by Cold Dark Matter and show, in their hotter phase (i.e. the hot Intra Cluster Medium – hereafter ICM – with temperature  $T_e \sim 10^7 - 10^8$  K), a complex temperature distribution in the cluster atmospheres as indicated by observations (see, e.g., Arnaud 2005 for a review; Pratt et al. 2007 for recent XMM-Newton results, Ehlert & Ulmer 2009 for recent Chandra results, Sato et al. 2009 for recent Suzaku results) and numerical simulations (see Borgani et al. 2008 for a recent review).

Spatially resolved studies of the ICM temperature distribution in galaxy clusters are crucial for both astrophysical and cosmological applications since these stud-

ies provide information on the thermodynamic state of the ICM, allow to measure the total mass of these systems through the hydrostatic equilibrium equation (see e.g. Arnaud 2005, Colafrancesco & Giordano 2007), and allow to set constraints on the relevant cosmological parameters ( $\Omega_m, \Omega_{DE}, \Omega_b$ ) through the study of the cluster population evolution.

On the cosmological side, once the gas mass is determined from X-ray observations in the deprojection or fitting analysis (see, e.g., Fabian et al. 1981; Ettori & Fabian 1999) and the total mass is estimated through the hydrostatic equilibrium condition, it is possible to derive the cluster gas mass fraction that can be used to constrain the cosmological density parameter, if combined with primordial nucleo-synthesis calculations (e.g., White et al. 1993, Ettori et al. 2009). Cosmological applications of the cluster population evolution require precise measurements of the cluster temperature and of the correlation be-

tween temperature and other relevant physical quantities, in order to describe correctly the cluster population (total mass, luminosity, Compton parameter, number counts, redshift distribution, luminosity function). If well calibrated, the slope and evolution of cluster scaling relations, such as gas mass versus temperature (e.g., Colafrancesco & Vittorio 1994, Colafrancesco et al. 1994, 1997, Voit 2000, Finoguenov, Reiprich, & Boehringer 2001) and cluster size versus temperature (e.g., Colafrancesco, et al. 1997, Mohr et al. 2000; Verde et al. 2001), can also be used to constrain cosmological and structure formation models.

On the astrophysical side, the precise determination of important quantities such as entropy, pressure, and – under the assumption of hydrostatic equilibrium – the total cluster mass, is dependent on accurate estimation of the temperature profile. Accurate temperature profiles are fundamental in determining the gas entropy distribution (see Lloyd-Davies, Ponman, & Cannon 2000 and references therein), which is a powerful tool to explore the role of non-gravitational processes that could alter the specific thermal energy in the ICM (Colafrancesco 2008a for a review, Kang et al. 2007, Colafrancesco & Giordano 2006, 2007), to assess the structure of cool cores and their surrounding atmosphere in order to probe the interplay of non-thermal and thermal particle distributions in clusters (e.g., Colafrancesco, Dar & DeRujula 2004, Guo & Ho 2008, Colafrancesco & Marchegiani 2008 and references therein) and to assess the amount of non-thermal (point-like and/or diffuse) emission mechanisms detectable in the hard X-ray domain (see discussion in Colafrancesco & Marchegiani 2009).

The standard methodology to recover the ICM temperature distribution makes use of high resolution spectroscopic X-ray observations (XMM, Chandra, Suzaku and previously ROSAT, ASCA, and BeppoSAX). Such observations provide the key measurable characteristics of the ICM, i.e., the temperature and density of this plasma. Because of limited photon statistics it is usual to measure the density and temperature in terms of radial profiles (see, e.g., Pratt et al. 2007). However, while the density of the ICM is relatively easy to measure from the surface brightness profile of a galaxy cluster, precise temperature determination requires high photon statistics to build, and fit, a spectrum. Therefore, ICM temperature profiles are typically determined with considerably less spatial resolution than density profiles. The measurement of radial temperature profiles is further complicated by the density squared dependence of the thermal bremsstrahlung X-ray emissivity,  $\varepsilon_{brem} \propto n_e^2(r)T_e^{1/2}(r)$ . The steep drop of the X-ray surface brightness with distance from the centre, combined with the background from cosmic, solar and instrumental sources, makes, hence, accurate X-ray measurement of the temperature distribution at large distances from the cluster centre a technically challenging task (see discussion in Pratt et al. 2007).

ICM temperature can also be measured, alternatively, by using the Inverse Compton scattering of CMB photons off thermal electrons residing in the cluster atmosphere – the Sunyaev-Zel'dovich effect (SZE; see Sunyaev & Zel'dovich 1980, Birkinshaw 1999, Colafrancesco 2007 for reviews). This effect provides a CMB temperature change

$$\frac{\Delta T}{T_0} = \frac{\sigma_T}{m_e c^2} \int_\ell d\ln_e k_B T_e \cdot g(x) \quad (1)$$

that depends on the cluster temperature  $T_e$  directly from its amplitude  $\propto y = \frac{\sigma_T}{m_e c^2} \int_\ell d\ln_e k_B T_e$  (where  $\sigma_T$  is the Thomson cross section,  $m_e$  is the electron mass,  $n_e$  is the electron density,  $T_e$  is the cluster temperature, the integral is performed along the line of sight  $\ell$ ), and from its spectrum  $\propto g(x)$  (where  $x \equiv h\nu/k_B T_0$  is the frequency normalized to the CMB energy,  $h$  is the Planck constant,  $k_B$  is the Boltzmann constant and  $T_0$  is the present-day CMB temperature). The temperature dependence is explicitly included in the function  $g(x)$  through the relativistic effects of the Compton Scattering that are more prominent in the high frequency region of the SZE spectrum at  $\nu \gtrsim 300$  GHz (see Birkinshaw 1999, Colafrancesco, Marchegiani & Palladino 2003, Colafrancesco 2007 for a review), where it is therefore possible to measure directly the ICM temperature. This is evident looking at the different temperature dependence of the three basic spectral features that characterize the thermal SZE signal:

i) the minimum in its intensity located at the frequency

$$x_{th,min} \approx 2.265(1 - 0.0927\theta_e + 2.38\theta_e^2) + \tau(-0.00674 + 0.466\theta_e), \quad (2)$$

where  $\theta_e \equiv k_B T_e / m_e c^2$ , whose value depends weakly on the electron spectrum (i.e. on  $T_e$  and  $n_e$ ) and equals  $\sim 2.26$ ;

ii) the crossover frequency,  $x_0$ , whose value depends on the electron pressure/energy density and optical depth

$$x_{th,0} \approx a(T_e) + \tau b(T_e) \quad (3)$$

with  $a(T_e) = 3.830(1 + 1.162\theta_e - 0.8144\theta_e^2)$  and  $b(T_e) = 3.021\theta_e - 8.672\theta_e^2$ , and is found at a frequency  $> 3.83$  for increasing values of  $T_e$  (the value  $x_{th,0} = 3.83$  is found in the non-relativistic limit, or in the limit  $T_e \rightarrow 0$ );

iii) the maximum of its intensity located at the frequency

$$x_{th,max} \approx 6.511(1 + 2.41\theta_e - 4.96\theta_e^2) + \tau(0.0161 + 8.16\theta_e - 35.9\theta_e^2) \quad (4)$$

and depends sensitively on the nature of the electron population and on its energy (momentum) spectrum (see Dolgov et al. 2001, Colafrancesco et al. 2003, Colafrancesco et al. 2009 for the case of electrons with a thermal spectrum; see also Colafrancesco et al. 2003 and Colafrancesco 2004, Colafrancesco 2005, Colafrancesco 2007, Colafrancesco 2008b for the case of electron with different spectra).

The SZE can be used, therefore, as an alternative probe of the ICM temperature provided that detailed

spectral measurements extending out to high frequencies can be obtained (see Colafrancesco 2007 for a review, see Colafrancesco et al. 2009).

The linear dependence of the SZE temperature change  $\Delta T$  from the electronic density  $n_e$  and temperature  $T_e$  (see eq. 1) makes it possible – in addition – to enhance the sensitivity of the SZE measurements in the outer regions of the cluster while maintaining an adequate sensitivity also in the inner parts. Therefore SZE observations could provide a more uniform and spatially extended coverage of the temperature profile in galaxy clusters than X-ray observations.

Little or nothing is known about cluster temperature profiles obtained directly from SZE observations. Present-day and planned SZE observations from both ground based experiments (multi-band bolometers and interferometers) or coming space-borne experiments (e.g., OLIMPO and PLANCK) require complementary X-ray observations to put tight constraints on the cluster temperature, even though a somewhat more moderate precision on cluster temperature seems to be sufficient to achieve a reasonable statistical knowledge on the CDM power spectrum, namely on  $\sigma_8$  (Juin et al. 2007).

We must also stress, in this context, that the use of X-ray observed quantities in the SZE data analysis is, however, a delicate procedure, because the SZE-derived temperature is weighted by the Compton parameter  $y$ . It is known, for instance, that the derived peculiar velocity is systematically shifted by  $\sim 10 - 20\%$  due to this reason (see e.g., Hansen 2004).

While observations of the SZE are becoming increasingly accurate (e.g., LaRoque et al. 2002; De Petris et al. 2002; Battistelli et al. 2003, Halverson et al. 2009, Staniszewski et al. 2009), most analyses of SZ data are still made under the simplifying assumption of iso-thermality, or single temperature plasma. Several studies have also considered the ability of future SZ observations to extract the cluster physical parameters (see, e.g., Knox, Holder & Church 2004; Aghanim, Hansen & Lagache 2005), but always under the assumption of iso-thermality.

A desirable solution with the SZE observations is to achieve simultaneous good angular resolution and high sensitivity in order to deproject the SZE signal properly throughout the whole cluster atmosphere.

In this paper we discuss specifically the strategy that will be more effective for obtaining spatially-resolved temperature measurements which are only based on SZE observations. Such strategy needs to overcome the following problems: i) achieve spatially resolved spectral measurements of the cluster temperature; ii) measure the temperature profile over a wide spatial range in order to disentangle the cool cores region from the outer cluster atmosphere (or regions with different temperature in the overall atmosphere); iii) obtain detailed and independent temperature measurements which require a wide frequency band coverage with sufficient spectral resolution. These points are the main issues that our study wants to address.

The outline of the paper is the following. We describe the general theory of the SZE in Sect.2, and we generalize this theory to the case of clusters with non-uniform T-profiles, like e.g. cool core clusters, in Sect. 3. We describe a fitting procedure for spatially resolved spectroscopic SZE observations in Sect.4, where we first discuss the case of the thermal SZE. The analysis of the non-thermal SZE and the combination of thermal and non-thermal SZE are also discussed, for completeness, in Sect.5. The non-thermal SZE is important both for the intrinsic study of non-thermal and/or relativistic plasmas in clusters and for determining their role as biases for the study of the thermal plasma (i.e. the ICM). We present in Sect. 6 the application of our study for two specific galaxy clusters: Perseus, which has a cool core, and Ophiuchus, which is approximately isothermal. We discuss our results and summarize our conclusions in the final Sect.7.

Throughout the paper, we use a flat, vacuum-dominated cosmological model with  $\Omega_m = 0.3$ ,  $\Omega_\Lambda = 0.7$  and  $H_0 = 70 \text{ km s}^{-1} \text{ Mpc}^{-1}$ .

## 2. The SZE: theory

In order to derive the expression of the SZE which is valid for a galaxy cluster with spatially varying density and temperature, we need to recall the general expressions for the SZE formulae.

We use here the formalism presented by Wright (1979), and subsequently developed by Birkinshaw (1999), Enßlin & Kaiser (2000), Colafrancesco, Marchegiani & Palladino (2003). We note that Böhm & Lavalle (2009) recently proposed a covariant formalism for the SZE, claiming, erroneously, that the formalism presented in Wright (1979) and further developed by other authors was incorrect. We have verified (both numerically and analytically) that the two approaches, in the Thomson limit, are fully equivalent and provide the same results (see Appendix A for details). In addition to our verification, Nozawa & Kohyama (2009) have also shown analytically that the two approaches are fully equivalent, pointing out the errors made by Böhm & Lavalle (2009).

The analytic expression for the upscattered CMB spectrum is:

$$I(x) = \int_{-\infty}^{+\infty} I_0(xe^{-s})P(s)ds \quad (5)$$

(see e.g. Colafrancesco, Marchegiani & Palladino 2003) where

$$I_0(x) = 2 \frac{(k_B T_0)^3}{(hc)^2} \frac{x^3}{e^x - 1} \quad (6)$$

with  $x = h\nu/k_B T_0$ .

The function  $P(s)$  is given by the following expression

$$P(s) = \sum_{n=0}^{+\infty} \frac{e^{-\tau} \tau^n}{n!} P_n(s), \quad (7)$$

where

$$\tau = \sigma_T \int_\ell n_e d\ell \quad (8)$$

is the electron optical depth and

$$P_n(s) = \underbrace{P_1(s) \otimes \dots \otimes P_1(s)}_{n \text{ times}} , \quad (9)$$

where the symbol  $\otimes$  indicates the convolution product, and

$$P_1(s) = \int_0^\infty f_e(p) P_s(s, p) dp . \quad (10)$$

The function  $f_e(p)$  is the electron momentum distribution function (with  $p = \beta\gamma$ ) and is normalized as to give  $\int_0^\infty f_e(p) dp = 1$ . The function  $P_s(s, p)$  is known from the basic physics of the Compton scattering and is given by

$$P_s(s, p) ds = P(e^s, p) e^s ds , \quad (11)$$

with

$$\begin{aligned} P(t, p) = & -\frac{3|1-t|}{32p^6t} [1 + (10 + 8p^2 + 4p^4)t + t^2] + \\ & + \frac{3(1+t)}{8p^5} \left[ \frac{3 + 3p^2 + p^4}{\sqrt{1+p^2}} + \right. \\ & \left. - \frac{3 + 2p^2}{2p} (2 \operatorname{arcsinh}(p) - |\ln(t)|) \right] . \end{aligned} \quad (12)$$

Our aim is to invert eq.(5) in order to derive the spectral and spatial parameters of the electrons distribution from measurements of the SZE only. We derive here an analytical solution to this problem, while in Sect. 4 we present a numerical procedure to solve it.

The approximated expression of  $\Delta I(x)$  at first order in  $\tau$  is

$$\Delta I(x) = \tau [J_1(x) - I_0(x)] \quad (13)$$

where

$$J_1(x) = \int_{-\infty}^{+\infty} I_0(xe^{-s}) P_1(s) ds . \quad (14)$$

Thus, by using eq.(10), we can write

$$\frac{\Delta I(x)}{\tau} + I_0(x) = \int_0^\infty k(x, p) f_e(p) dp , \quad (15)$$

where

$$k(x, p) = \int_{-\infty}^{+\infty} I_0(xe^{-s}) P_s(s, p) ds . \quad (16)$$

Introducing the following definitions

$$\mathcal{H}f_e(x) \equiv \int_0^\infty k(x, p) f_e(p) dp \quad (17)$$

$$\tilde{I}_\tau(x) \equiv \frac{I(x)}{\tau} + I_0(x) , \quad (18)$$

the previous eq.15 writes as

$$\tilde{I}_\tau(x) = \mathcal{H}f_e(x) . \quad (19)$$

Its formal solution is given by

$$f_e(x) = \mathcal{H}^{-1}\tilde{I}_\tau(x) \quad (20)$$

with

$$\mathcal{H}^{-1}\mathcal{H} = \mathcal{I} , \quad (21)$$

where  $\mathcal{I}$  is the identity operator.

### 3. The SZE for a galaxy cluster with a radial temperature profile

In order to apply the general formalism described in the previous Section to a cluster with a spatially varying temperature and density profiles (i.e., a cluster with a cool core or a non-isothermal cluster), we must consider that:

- equations (5)–(9) still hold. In particular, the expression for the optical depth remains the same because it depends only on the gas density profile and not on the cluster temperature;
- the expression for the function  $P(s)$ , and its series expansion in terms of powers of  $\tau$ , remains formally unchanged, because it gives the probability that a CMB photon suffers a (logarithmic) change in the frequency  $s \equiv \ln(\nu'/\nu)$  by traversing the whole cluster;
- the expression for the function  $P_1(s)$  (i.e. eq. 10) must be changed. In fact, the expression given in eq.(10) assumes that the electron momentum distribution function  $f_e(p)$  is the same throughout the cluster atmosphere. Such an assumption is not correct for a cluster with a cool core (or a non-isothermal cluster) since its temperature, and hence the electron momentum distribution, changes with the cluster radius.

We must, therefore, find an appropriate way to calculate the function  $P_1(s)$  taking into account the fact that the CMB photon, while traversing the cluster atmosphere, finds regions with different temperature and density. In order to calculate the redistribution function  $P_1(s)$  appropriately, we can calculate – along the line of sight  $\ell$  – the local electron momentum distributions weighted by its local density.

Describing the thermal electron density as

$$n_e(r) = n_{e0} \cdot g_e(r) , \quad (22)$$

it is possible to derive the average density-weighted momentum distribution along the line of sight  $\ell$  as

$$\bar{f}_e(p) \equiv \frac{\int_\ell f_e(p; T_e(r)) g_e(r) d\ell}{\int_\ell g_e(r) d\ell} , \quad (23)$$

where

$$f_e(p; T_e) = \frac{\eta}{K_2(\eta)} p^2 \exp\left(-\eta\sqrt{1+p^2}\right) , \quad (24)$$

with  $\eta = (m_e c^2)/(k_B T_e)$  and  $K_2(\eta)$  being the modified Bessel function of second kind (see, e.g., Abramowitz & Stegun 1965), which ensures the correct normalization

$$\int_0^\infty f_e(p; T_e) dp = 1. \quad (25)$$

The function  $\bar{f}_e$  also satisfies the normalization given in eq.(25), as can be verified by the following equation

$$\begin{aligned} \int_0^\infty \bar{f}_e(p) dp &= \frac{\int_0^\infty dp \int_\ell f_e(p; T_e(r)) g_e(r) d\ell}{\int_\ell g_e(r) d\ell} = \\ &= \frac{\int_\ell g_e(r) d\ell \int_0^\infty dp f_e(p; T_e(r))}{\int_\ell g_e(r) d\ell} = \\ &= 1, \end{aligned} \quad (26)$$

where we use eq. (25).

We can, therefore, re-write eq.(10) for a cluster with a generic temperature distribution by using the averaged electron momentum distribution

$$P_1(s) = \int_0^\infty \bar{f}_e(p) P_s(s, p) dp, \quad (27)$$

where  $\bar{f}_e(p)$  is given in eq.(23). This function allows us to calculate the frequency redistribution probability for multiple scattering and, hence, the analytic expression of the SZE up to the required approximation order by using eqs. (5)–(9).

#### 4. Fitting procedure: the thermal SZE

Eq.(20) cannot be easily solved by analytically methods. Therefore, we describe in this section a numerical procedure by which it is possible to derive the cluster temperature profile starting from observations of the SZE with appropriate spatial and spectral resolution.

The quantitative analysis that we present here refers to the specific case of the cluster A2199 which has a cool core.

The procedure that we follow consists of simulating the thermal SZE observation of the cluster A2199 with parameters (density and temperature) taken from the available X-ray observations, and then extract the best fit values of the ICM temperature and optical depth from the simulated SZE observations. Note that in this section we work, for convenience, with the first-order approximation to the thermal SZE, and in Sect.5 we will discuss the consequences of using this approximation. The temperature profile obtained from SZE measurements taken at various cluster radii is then de-projected under the constraint (prior) that the density profile derived from SZE observations is consistent with the density profile obtained from X-ray measurements: we use this procedure (which hence assumes the X-ray density prior) in order to have a fast enough computing time that allows us to explore the details of our study. Note, however, that the density constraint is not necessary, in principle, because the cluster density profile can be obtained, self-consistently, from the

optical depth profile measured from SZE measurements. This fully consistent procedure requires, however, much longer computing times since the number of free parameters to be fitted to the observations is larger.

For the reference case of A2199 that we want to discuss in this section, our analysis goes through the following steps: i) we have taken X-ray information on A2199 from Chandra observation (Johnstone et al. 2002); ii) using the density and temperature profiles derived from X-ray observations we calculated (using the procedure described in Sect.3 above) the SZE spectrum at eight different projected radii  $r_p$  from the cluster center, i.e.,  $r_p = 0, 5, 10, 15, 20, 30, 50$  and 100 kpc; iii) for each radial bin, we have sampled the SZE spectrum at six different frequencies, i.e.  $\nu = 300, 320, 340, 360, 380$  and 400 GHz (see Fig. 1); iv)

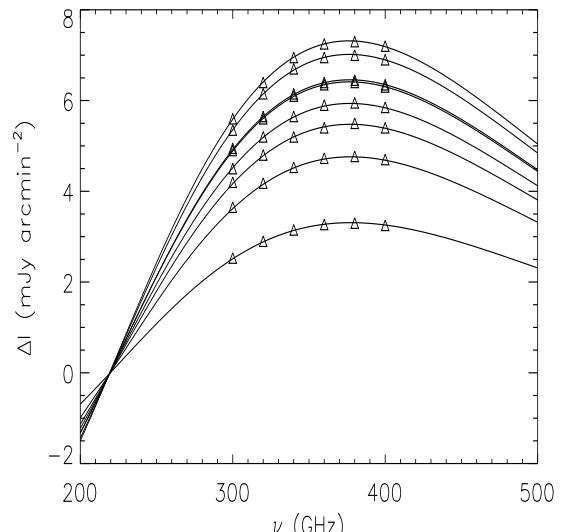


**Fig. 1.** The SZE spectrum obtained for the cluster A2199 at different projected radii is shown together with the frequency sampling derived, for each curve, with a 0.1% uncertainty. From top to bottom curves refer to projected radii of 0, 5, 10, 15, 20, 30, 50, 100 kpc. Note that spectra for 10 and 15 kpc are almost superposed due to the fact that beyond this radial distance the IC gas temperature measured by Chandra decreases with increasing radius (Johnstone et al. 2002).

for each radius, we fitted the six frequency SZE data with a relativistic model of the thermal SZE leaving two parameters, i.e.  $k_B T_e$  and  $\tau$ , and assuming for each experimental data point an uncertainty of 0.1%. This fitting procedure yields, for each projected radius, a value of the projected temperature and optical depth (see Fig. 2); v) in order to deproject the fitted temperature profile, we have assumed a 3-D theoretical temperature profile of the form:

$$T_e(r) = T_{int} + (T_{ext} - T_{int}) \frac{(r/r_c)^\mu}{1 + (r/r_c)^\mu} \quad (28)$$

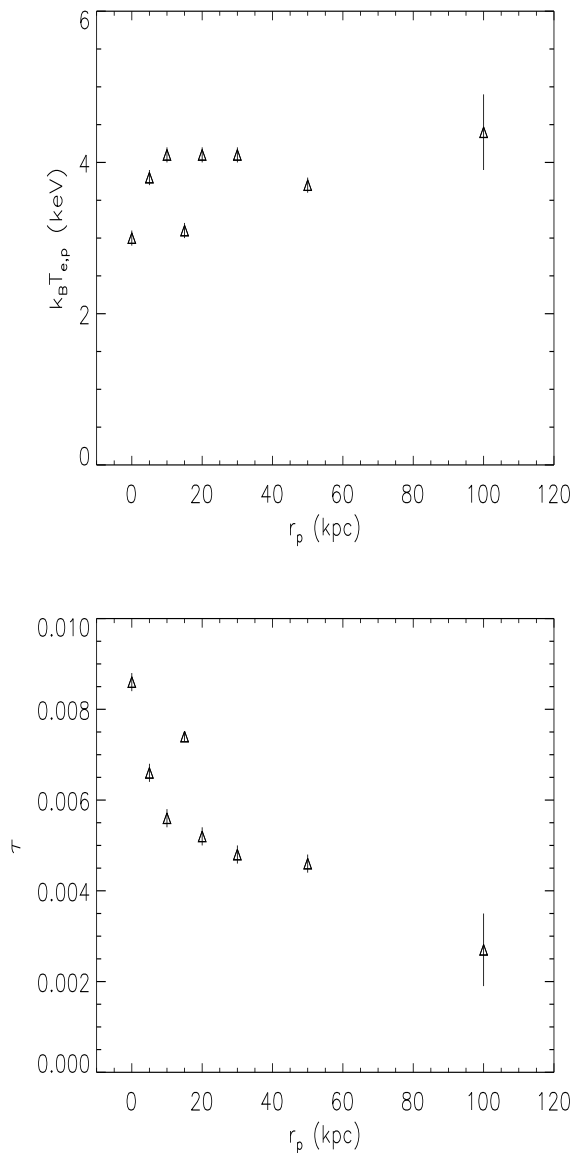


**Fig. 2.** The radial profile of the projected temperature (top panel) and optical depth (bottom panel) as derived from the fit to the SZE spectra using data sampled in the frequency range 300–400 GHz with uncertainty of 0.1% (see Fig.1).

(see e.g. Piffaretti et al. 2005). To decrease the number of free parameters in the fit we have assumed the ICM density profile  $n_e(r)$  as obtained from X-ray data. In the fitting procedure, the projected temperature is calculated by weighting the temperature profile with the gas density and integrating along the los:

$$T_{e,p}(r_p) = \frac{2 \int_0^R n_e(r) T_e(r) \frac{r}{\sqrt{r^2 - r_p^2}} dr}{2 \int_0^R n_e(r) \frac{r}{\sqrt{r^2 - r_p^2}} dr}, \quad (29)$$

where  $R$  is the cluster radius (and it is  $R = 200$  kpc for the case of A2199). Assuming the value of  $T_{ext}$  from X-ray observations, the number of free parameters reduces

to three. In this way it is possible to fit the projected temperature as obtained from the simulated SZE observations and then derive the temperature profile parameter (in eq.28); assuming  $k_B T_{ext} = 4.2$  keV for the case of A2199, the best fit parameters are  $k_B T_{int} = 0.0 \pm 0.5$  keV,  $r_c = 4.9 \pm 0.6$  kpc and  $\mu = 1.0 \pm 0.1$ . The best-fit temperature profile curve is shown in Fig.3 and it is compared to the data on the de-projected temperature as derived from X-ray observations.

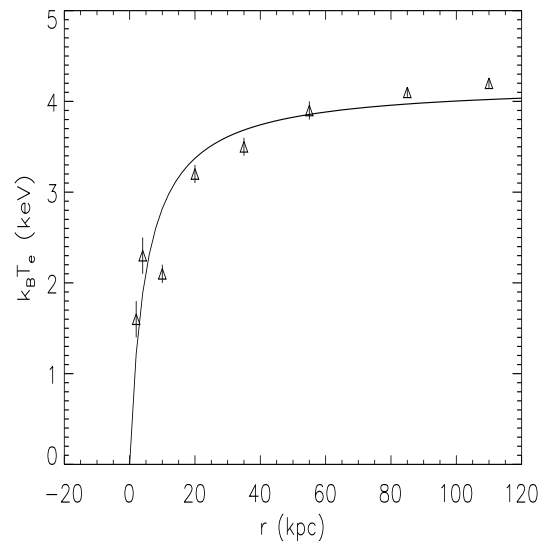


**Fig. 3.** The deprojected temperature profile curve (solid) derived from SZE spectral data is compared with the deprojected temperature data as obtained from X-ray measurements of A2199 (Johnstone et al. 2002).

The same procedure has been also repeated assuming that the SZE observation sampled from Fig. 1 has an uncertainty of 1%. The radial profile of the projected temperature obtained in this case is shown in Fig. 4. In this case, the de-projection of the temperature profile using the template given in eq. (28) does not provide, however, an acceptable fit. For this reason we conclude that an uncertainty of order of 1% in the SZE data is not sufficient to derive a detailed profile of the ICM temperature in clusters like A2199.

The whole procedure has been repeated sampling the SZE observations in the low-frequency range 100–200 GHz ( $\nu = 100, 120, 140, 160, 180, 200$  GHz). In such a case, we find that, even assuming uncertainties of 0.1%, it is not possible to reproduce in a satisfactory way the radial profile of the projected temperature as derived from the fit by using the model in eq.(28) (see Fig.5). This is because the shape of the SZE spectrum at low frequencies is less sensitive to the cluster temperature than the shape of the high-frequency part of the SZE spectrum. Therefore, in order to obtain detailed information on the cluster temperature profile one must use high-frequency spectral observations

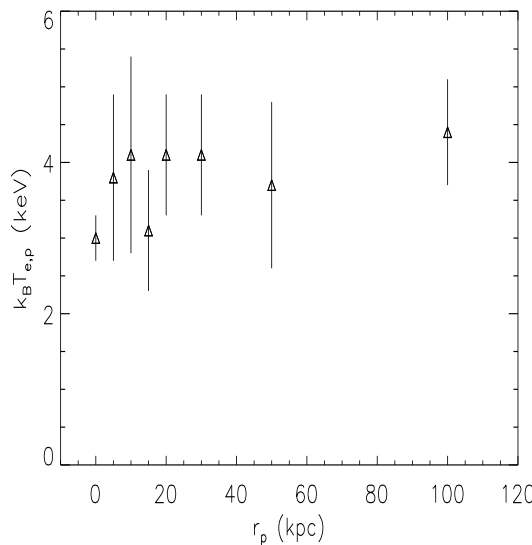


**Fig. 4.** The projected temperature profile obtained from the fit to SZE spectra using data points sampled in the 300–400 GHz range and assuming an uncertainty of 1%.

in the range 300–400 GHz. This is a crucial requirement to plan an observational strategy of SZE observations with the goal of deriving strong constraints to the fundamental parameters of the cluster.

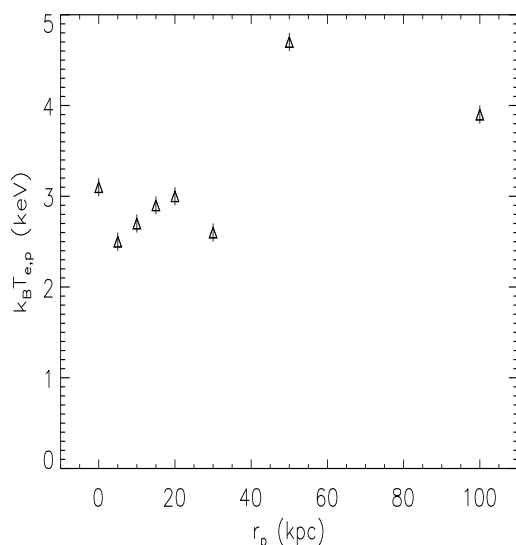


**Fig. 5.** The projected temperature radial profile obtained from the fit to the SZE spectral data by using data points sampled in 100–200 GHz range and assuming uncertainties of 0.1%.

## 5. Fitting procedure: the non-thermal SZE

Here we consider the effects of the variation of the parameters of the non-thermal electron spectrum on the relative non-thermal SZE.

First, we study the spectral shape of the non-thermal SZE as a function of the electrons spectral parameters. In this case, we use an arbitrary normalization in which the amplitude of the SZE at its minimum is set equal to  $-1$ , and we vary the parameters of the electrons spectrum. Fig.6 shows the SZE spectrum for a single power-law spectrum

$$f_e(p) \propto p^{-s_1}; \quad p \geq p_1 \quad (30)$$

(here  $p = \beta\gamma$  is the normalized momentum), with  $s_1 = 3.0$ , as a function of the minimum momentum  $p_1$ . It is clear that the frequency position of the minimum of the SZE is different in the case  $p_1 = 1$ , while for  $p_1 \geq 5$  the position of the minimum does not change for different values of  $p_1$ . The shape of the spectrum at higher frequencies ( $\nu \geq 300$  GHz) is, instead, more sensitive to the value of  $p_1$ .

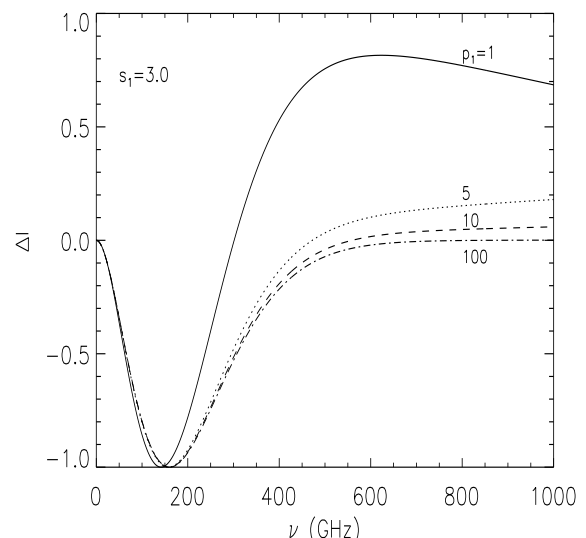


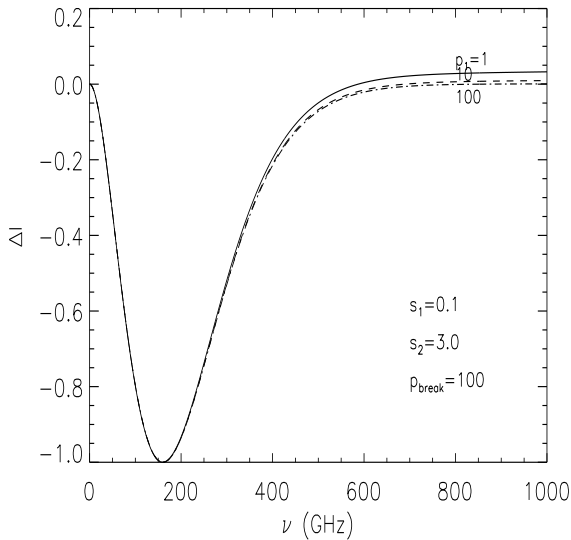
**Fig. 6.** The non-thermal SZE spectrum, normalized to its minimum amplitude is shown as a function of the minimum momentum  $p_1$  of the electron spectrum. We assume here a single power-law spectrum with  $s_1 = 3.0$ .

We show in Fig.7 the case of a double power-law spectrum

$$f_e(p) \propto \begin{cases} p^{-s_1} & p_1 \leq p \leq p_{break} \\ p_{break}^{-s_1} (p/p_{break})^{-s_2} & p > p_{break} \end{cases} \quad (31)$$

with  $s_1 = 0.1$ ,  $p_{break} = 100$  and  $s_2 = 3.0$ . In this case the position of the minimum and the shape of the spectrum at frequencies  $\nu \leq 400$  GHz, depends weakly from the value of  $p_1$ , while a stronger dependence from  $p_1$  is present at higher frequencies (this dependence is anyway weaker than

for the single power-law case because of the lower power at the low- $p$  end of the electron spectrum).



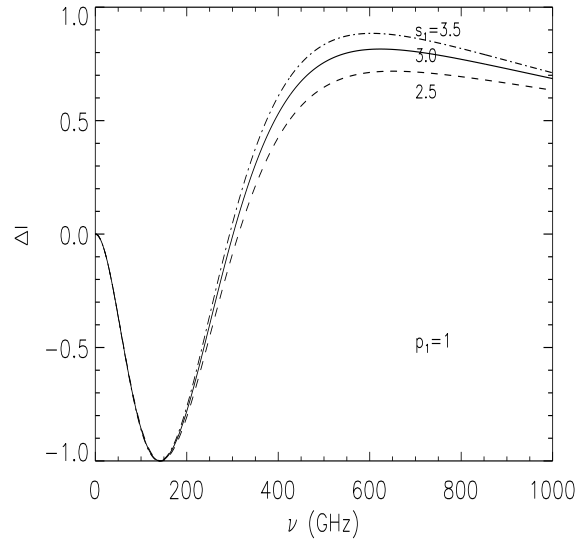
**Fig. 7.** The non-thermal SZE spectrum, normalized to its minimum amplitude is shown as a function of the minimum momentum  $p_1$  of the electron spectrum. We assume here a double power-law spectrum with  $s_1 = 0.1$ ,  $s = 3.0$  and  $p_{\text{break}} = 100$ .

Fig.8 shows the changes of the SZE spectrum in the case of a single power-law with  $p_1 = 1$  as a function of the spectral index  $s_1$ : also in this case the shape of the SZE spectrum is more sensitive to the shape of the electron spectrum at frequency  $\nu \geq 400$  GHz. Fig.9 show the variation of the SZE spectrum as a function of the spectral index  $s_2$  for a double power-law spectrum: in this case the dependence from the electron spectrum index is quite weak for the considered frequency range.

After having shown the dependence of the SZE spectrum on the electron spectrum parameters, we discuss now the procedures through which we can recover the physical parameters of the non-thermal electron spectrum from the SZE observations. We consider here two cases: i) the case of a pure non-thermal electron population with a power-law spectrum (a situation applicable to radio galaxy lobes, see e.g. Colafrancesco 2008b); ii) the case of a combination of thermal plus non-thermal electron population with a double power-law spectrum (a situation applicable to galaxy clusters with non-thermal phenomena, see e.g. Colafrancesco et al. 2003).

### 5.1. The case of a single power-law spectrum

We describe here the procedure through which it is possible to derive the parameters of an electron population with single power-law spectrum, assuming that this is the dominant electron population for the SZE production.



**Fig. 8.** The non-thermal SZE spectrum, normalized to its minimum amplitude is shown as a function of the spectral index  $s_1$  of the electron spectrum. We assume here a single power-law spectrum with  $p_1 = 1$ .

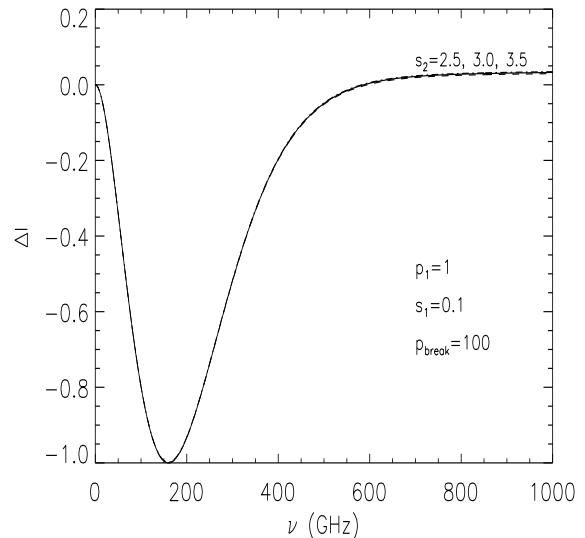


**Fig. 9.** The non-thermal SZE spectrum, normalized to its minimum amplitude is shown as a function of the spectral index  $s_2$  of the electron spectrum. We assume here a double power-law spectrum with  $p_1 = 1$ ,  $s_1 = 0.1$  and  $p_{\text{break}} = 100$ .

Following the same procedure previously outlined for the thermal SZE in Sect.4, we have sampled the non-thermal SZE produced at different projected radii and at six frequencies in the range 300 – 400 GHz where, as previously noticed, the shape of the SZE is maximally sensitive to the physical parameters of the electron spectrum. The emission region has been assumed, for simplicity, to have

spherical symmetry with a radius of 50 kpc with an electron spectrum

$$N_e(p, r) = k_0 p^{-s_1} \cdot g_e(r) \quad p \geq p_1 \quad (32)$$

Here we assume  $s_1 = 3.0$ ,  $p_1 = 3$ ,  $k_0 = 10^{-2} \text{ cm}^{-3}$  and a radial distribution of the electron population given by

$$g_e(r) = \left[ 1 + \left( \frac{r}{r_c} \right)^2 \right]^{-q_e} \quad (33)$$

with  $r_c = 10$  kpc and  $q_e = 0.5$ .

In the fitting procedure we discuss here, we fix the spectral index of the electron spectrum  $s_1$ , because it can be derived from radio observations, and we fit the simulated observations with two free parameters: the optical depth  $\tau$  and the minimum momentum  $p_1$ . We note that the assumption of the parameter  $s_1$  from radio data is not strictly necessary, because, in the presence of adequate coverage in frequency, it can be derived from the SZE data alone; this assumption is made for the sole purpose of reducing the time of calculation.

The SZE intensity at different radii and the relative sampling are shown in Fig.10. The behaviour of the optical

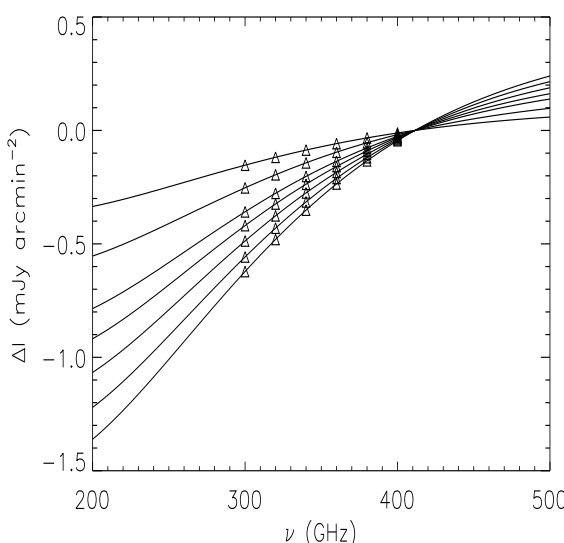


**Fig. 10.** The non-thermal SZE spectrum evaluated at various projected radii and frequency sampling (see text for details) with data uncertainty of 0.1%. Curves are, from bottom to top, for projected radii of 0, 5, 10, 15, 20, 30, 40 kpc.

depth at different projected radii, as derived by the fitting procedure, is shown in Fig. 11. Our analysis recovers the values  $p_1 = 3.1 \pm 1.0$  at all the considered projected radii. In order to deproject the optical depth radial distribution and derive the radial profile of the electron density it is sufficient to fit the optical depth profile with a density profile as in eq. (33) and integrate along the line of sight. The deprojection procedure yields  $k_0 = (9.0 \pm 3.5) \times 10^{-3}$

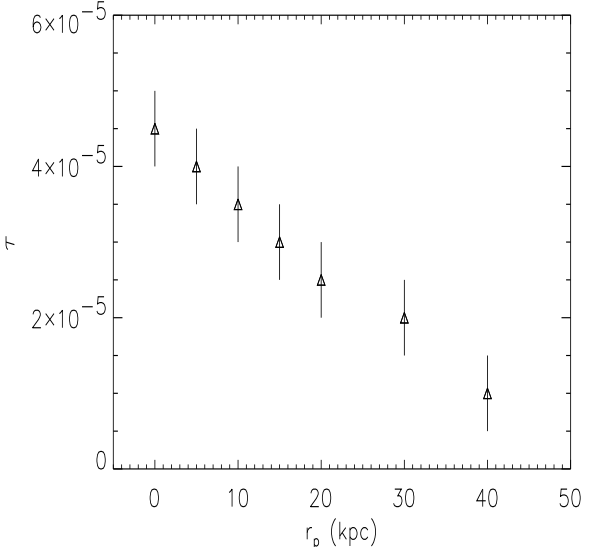


**Fig. 11.** The radial profile of the optical depth as obtained from the fit to the SZE spectra b using data sampled in the range 300–400 GHz with uncertainty of 0.1% (see Fig.10).

$\text{cm}^{-3}$ ,  $r_c = 7.2 \pm 6.0$  kpc and  $q_e = 0.43 \pm 0.21$ ; these values are consistent, within the errors, with the input values that we used in the simulations.

We stress that the previous analysis of the SZE spectral measurements allows to derive directly the density profile and the spectral shape of the electron distribution in the radio lobes. Therefore, the combination of SZE spectral measurements and measurement of the low-frequency radio emission allows to break the degeneracy existing in synchrotron emission between the electron density and the magnetic field and eventually yield a measure of the magnetic field in radio lobes (see also Colafrancesco 2008b).

## 5.2. The case of thermal plus non-thermal populations

Here we consider a combination of a thermal electron distribution that fits the A2199 data and an additional non-thermal electron spectrum with a double power-law spectrum, as in eq.(31), with parameters  $s_1 = 0.1$ ,  $s_2 = 3.0$ ,  $p_1 = 1$  and  $p_{\text{break}} = 100$ .

A non-thermal electron spectrum similar to a double power-law is expected in galaxy clusters because the non-thermal electrons of relatively low energy loose energy through Coulomb interactions with the thermal IC gas, and these energy losses produce a flattening of the electron spectrum at low ( $\lesssim 150$  MeV) energies. To study this case, we do not follow the same strategy described in the previous Sections: specifically, we do not perform a fit to the sampled points because this procedure should involve too many free parameters (i.e., those of both the thermal and the non-thermal electron populations). Instead, we focus on the spectral regions where the non-thermal effect is expected to be more relevant, and

therefore it can be measured. For this purpose, we compare the non-thermal SZE spectrum with the thermal SZE spectrum (calculated both at first order in  $\tau$  and with second order corrections, see Sect.2 and Colafrancesco et al. 2003 for more details), and with the spectrum of a possible SZ kinematic effect. The spectral regions where the non-thermal SZE could be better estimated are the frequency range around the minimum of the SZE (at  $\nu \sim 150$  GHz), because all the amplitudes are basically proportional to the optical depth of the relative electronic population, and the frequency range around the crossover frequency of the thermal SZE (at  $\nu \sim 220$  GHz), because the thermal SZE is by definition null at such frequency leaving hence visible the (negative in sign) non-thermal SZE.

We note that an upper limit to the non-thermal electron density can be derived, after fixing their spectral shape, by requiring that the non-thermal pressure does not exceeds the thermal one (see discussion in Colafrancesco et al. 2003). Fig.12 shows the ratio between the non-thermal SZE and the thermal SZE in the case  $P_{nt} \sim P_{th}$  at the cluster center: this case can be considered as an upper limit to the contribution of the non-thermal component to the total SZE. Fig. 13 shows the spectrum of the thermal and non-thermal SZE in the frequency ranges 100–200 GHz and 300–400 GHz. The ratio of the non-thermal to the thermal SZE is large only in the region around  $\nu \sim 220$  GHz where the thermal SZE has its crossover and where, consequently, the total SZE is dominated by the non-thermal component. For  $\nu < 200$  GHz the non-thermal SZE is  $\sim 1\%$  of the thermal one, while for  $\nu > 300$  GHz the ratio becomes very low, of order of  $\sim 0.1\text{--}0.5\%$ , or even less. Two conclusions can be derived from these results: 1) In the frequency range 300–400 GHz, that is optimal to derive precise information on the thermal SZE, the non-thermal component does not provide a contribution that jeopardizes the precision of the measurements. 2) At lower frequencies, around 200 GHz, the contribution of the non-thermal component is more relevant; however, to determine such a component, it is necessary to separate it from the thermal one.

A possible observational strategy to separate the non-thermal effect from the thermal one could consist in measuring the thermal SZE in the frequency range 300–400 GHz and deriving the IC gas physical parameters, as seen in Sect.4. Then, once the thermal SZE parameters are fixed, it will be possible to measure the SZE in the frequency range 100–200 GHz and derive the parameters of the non-thermal population that, in this frequency range, yields a contribution to the total SZE of order of  $\sim 1\%$  (see figures 12 and 13): such SZE amplitude is measurable if measurements have an uncertainty of order of  $\sim 0.1\%$ .

For a precise determination of the cluster parameters, we must take into account the contribution of the thermal SZE evaluated at second order in  $\tau$ ; this can be calculated in details once the main parameters of the IC gas are known (see Colafrancesco et al. 2003 for details). The modifications induced by the second order effect, in comparison to the non-thermal SZE and to the first-order ther-

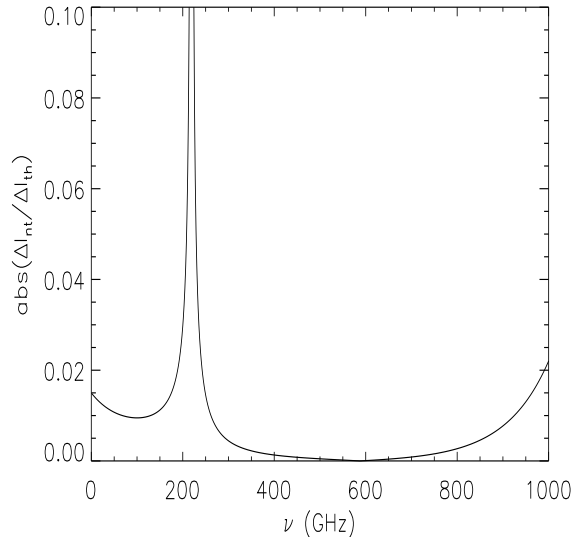


**Fig. 12.** The frequency dependence of the ratio of the non-thermal SZE (we assume a double power-law spectrum with  $s_1 = 0.1$ ,  $s_2 = 3.0$ ,  $p_1 = 1$  and  $p_{break} = 100$ ) to the thermal SZE at the center of A2199. We assume a pressure balance  $P_{nt} \sim P_{th}$  at the cluster center.

mal SZE, are shown in Fig. 14. For the frequency range 300–400 GHz, that is the optimal frequency window to extract the thermal SZE parameters, the second-order correction to the thermal SZE is less than 30% of the non-thermal SZE and it is less than 0.1% of the first-order thermal SZE. Hence, we can conclude that the total SZE can be adequately approximated, in this frequency range, by the first-order thermal SZE only. Moreover, in the frequency range 100–200 GHz, where the non-thermal effect could be measured, the second order correction to thermal effect is  $\sim 5\%$  of the non-thermal effect, so that the second order correction can be neglected also for this purpose.

We consider now also the possible contribution of a kinematic SZE whose amplitude is maximal at frequency around the crossover frequency of the thermal SZE, i.e. at  $\nu \sim 220$  GHz. Fig. 15 shows the ratio of the kinematical to the non-thermal SZE (upper panel) and the ratio of the kinematical to the thermal SZE (lower panel) for a receding cluster with peculiar velocity of 1000 km/s. The result is that in the frequency range 300–400 GHz also the kinematical contribution is a small fraction ( $\sim 20\%$ ) of the non-thermal SZE, and it is less than 0.1% of the thermal one. Therefore, also the kinematical SZE can be neglected in this frequency range.

Fig. 15 also shows that in the range 100–200 GHz the kinematical SZE is less than 10% of the non-thermal SZE. However, if the non-thermal electron population have a pressure  $P_{nt} \sim 0.1P_{th}$ , then the non-thermal and kinematical SZE would become comparable (under the assumption of having  $V_p = 1000$  km/s); in such a case, however, these signals would be indistinguishable from the thermal one

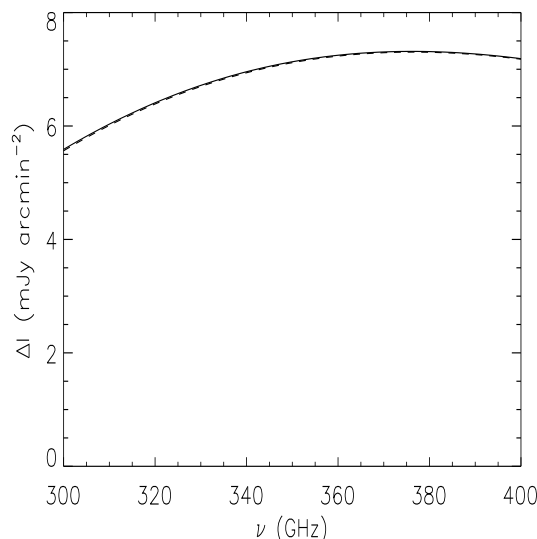
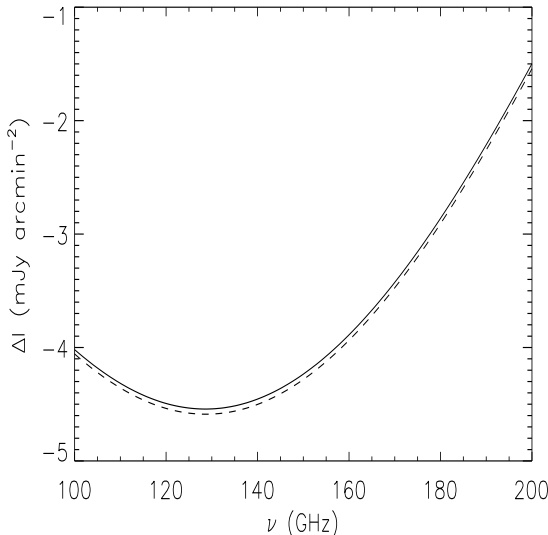


**Fig. 13.** The thermal (solid curve) and non-thermal (dashed curve) SZE evaluated at the center of A2199. The non-thermal electron population has a double power-law spectrum with parameters  $s_1 = 0.1$ ,  $s_2 = 3.0$ ,  $p_1 = 1$  and  $p_{break} = 100$  and a pressure  $P_{nt} \sim P_{th}$  at the cluster center. The spectra are shown in the frequency range 100–200 GHz (upper panel) and 300–400 GHz (lower panel).

(see for reference, Figs. 12 and 13 upper panel, in which we show the case  $P_{nt} \sim P_{th}$ ).

We can summarize the results obtained:

- in the frequency range 300–400 GHz, the first order thermal SZE is a good approximation of the total SZE (all the corrections are  $\leq 0.1\%$ ).
- in the frequency range 100–200 GHz, if the non-thermal contribution is strong, it dominates over the kinematic one. If, instead, the two SZE contributions are comparable, then they cannot be easily disentangled from the

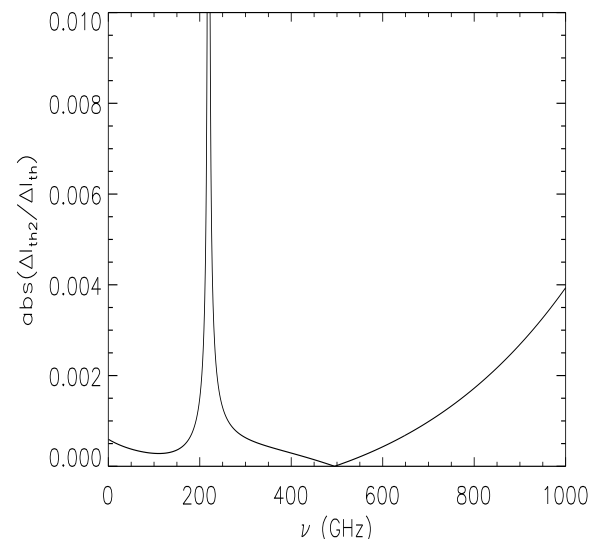
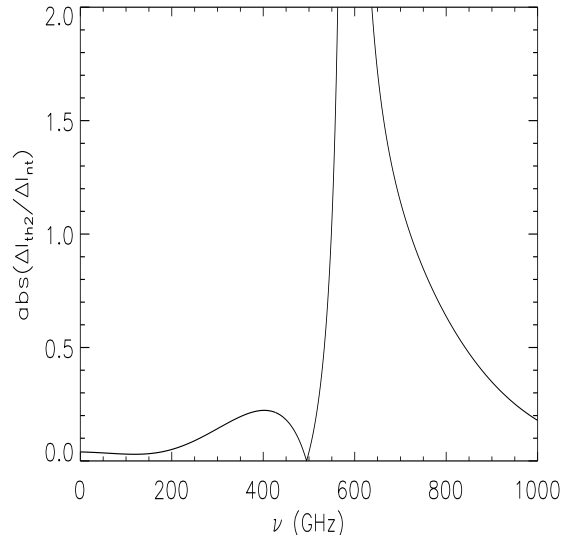


**Fig. 14.** Upper panel: the frequency dependence of the absolute value of the ratio between the second order correction to the thermal SZE at the center of A2199 and the non-thermal SZE of an electron population with double power-law spectrum with parameters  $s_1 = 0.1$ ,  $s_2 = 3.0$ ,  $p_1 = 1$ ,  $p_{break} = 100$  and with pressure  $P_{nt} \sim P_{th}$ . Lower panel: the frequency dependence of the ratio between the second order correction and the first order description of the thermal SZE.

thermal one. Hence, if deviations from expected thermal SZE are measured in this frequency range, they should be of non-thermal origin.

- only at  $\nu \sim 220$  GHz (i.e. the crossover frequency of thermal SZE) the kinematic SZE, the non-thermal one and the second order thermal correction are important with respect to the first order thermal effect. To disentangle between the three different contributions it is important to put constraints on the thermal and the non-thermal pa-

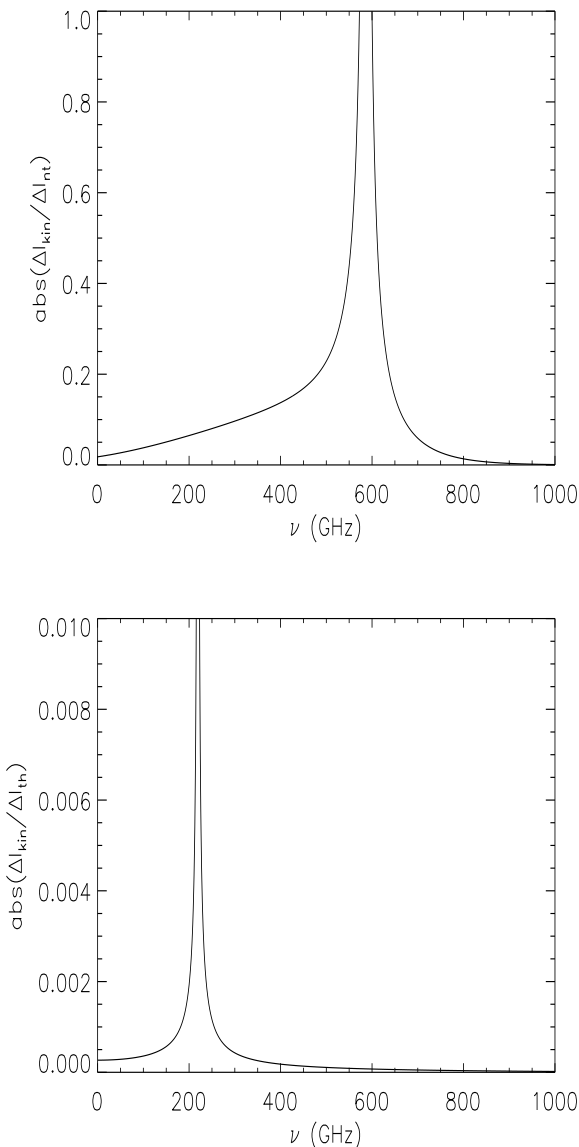


**Fig. 15.** Upper panel: the frequency dependence of the absolute value of the ratio between the kinematic SZE for a value of the peculiar velocity of  $v_p = 1000$  km/s and the non-thermal SZE for an electron population with the same spectrum as in Fig. 14. Lower panel: the frequency dependence of the absolute value of the ratio between the kinematic SZE and the thermal SZE evaluated at first order.

rameters by performing precise observations in frequency ranges 300–400 and 100–200 GHz, respectively.

## 6. Applications to specific clusters: Perseus and Ophiuchus

We present in this section the results of our studies for two nearby and extended clusters: Perseus, which has a cool core, and Ophiuchus, which is approximately isothermal. As we discussed in the previous sections, the optimal strategy to extract the physical parameters of the cluster

is to consider the frequency range 300–400 GHz; in this range, we can safely consider only the first order thermal SZE in our analysis, because higher-order corrections are negligible.

### 6.1. The Perseus cluster

The Perseus cluster is at a redshift  $z = 0.0179$  or at a distance of 77.7 Mpc, at which 1 arcmin corresponds to 21.8 kpc. Therefore, a study of the spatially resolved SZE allows to have a spatial sampling of the temperature profile better than in the case of A2199 previously discussed. In the following, we repeat the previous analysis for this cluster.

Churazov et al. (2003) derived an analytical approximation for the radial profile of the IC gas density and of the gas temperature that fits the cluster data for  $r > 10$  kpc, while at shorter distances the presence of the central dominating galaxy NGC1275 makes the IC gas radial profile more uncertain. Here, for sake of illustration, we use the analytical fitting formulae given by Churazov et al. (2003) and we extrapolate them down to the cluster center, e.g. ignoring, in this way, the presence of the central galaxy.

We have hence simulated the thermal SZE to first order expected from Perseus at seven projected radii from the cluster center: 0, 20, 50, 75, 100, 150 and 200 kpc (corresponding to angular sizes of 0, 0.9, 2.3, 3.4, 4.7, 6.9 and 9.2 arcmin). We have then sampled each one of the SZE spectra at these radii for eight different frequencies: 300, 320, 340, 360, 380, 400, 420 and 440 GHz (see Fig. 16). We have extended the frequency coverage in order to better sample the spectral region of the SZE where relativistic effects are relevant. For each projected radius we have finally fitted, using the gas temperature and optical depth as free parameters, the SZE simulated signal by using the expression of the first-order thermal SZE and assuming an error of 1% in the experimental data. The results of the fit for the projected temperature are shown in Fig. 17. The deprojection procedure of the best-fit radial temperature profile is done by using Eq. (28) setting the values  $k_B T_{\text{ext}} = 6.8$  keV (the best-fit projected temperature at 200 kpc), and by using as prior constraints the information on electrons radial profile provided by X-rays observations (see Sect. 4); for an experimental uncertainty of 1%, such procedure yields values  $k_B T_{\text{int}} = 3.6 \pm 1.5$  keV,  $r_c = 104 \pm 45$  kpc,  $\mu = 4.0 \pm 2.4$ , with  $\chi^2 = 0.1$  for 4 d.o.f. Fig. 18 shows the comparison between the deprojected temperature profile found with our method and the best-fit deprojected temperature profile derived by Churazov et al. (2003). The two curves are quite similar except for the inner region where the IC gas is cooler and the sensitivity of the SZE spectrum to low temperatures (through the effect of relativistic corrections) is lower. We have also verified that assuming an uncertainty of 0.1% in the experimental data, the best-fit values do not change, while the relative errors are considerably reduced (see Fig. 19).

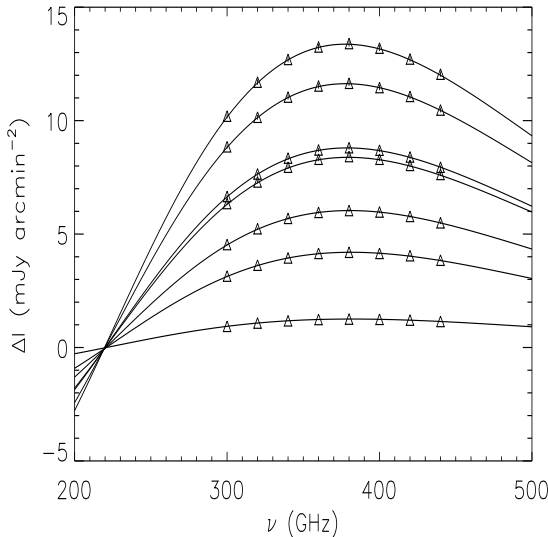


**Fig. 16.** The thermal SZE spectra of the Perseus cluster evaluated at different projected radii of 0, 20, 50, 75, 100, 150 e 200 kpc (from top to bottom) are shown in the frequency range 200–500 GHz. For each curve the SZE sampling in the frequency range 300–450 GHz has an uncertainty of 1%.

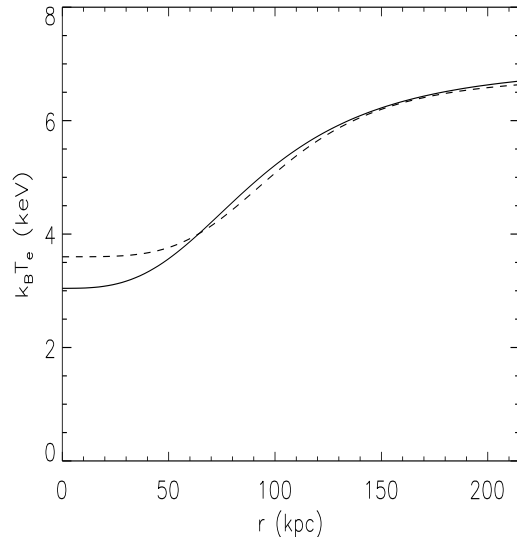


**Fig. 18.** The deprojected temperature radial profile in Perseus derived from the fit to the X-ray data by Churazov et al. (2003) (solid curve) is compared to the fit to the SZE simulated data (dashed curve) shown in Fig. 17. For the SZE temperature profile we use the radial profile given by eq. (28), with  $k_B T_{ext} = 6.8$  keV,  $k_B T_{int} = 3.6$  keV,  $r_c = 104$  kpc and  $\mu = 4.0$ .

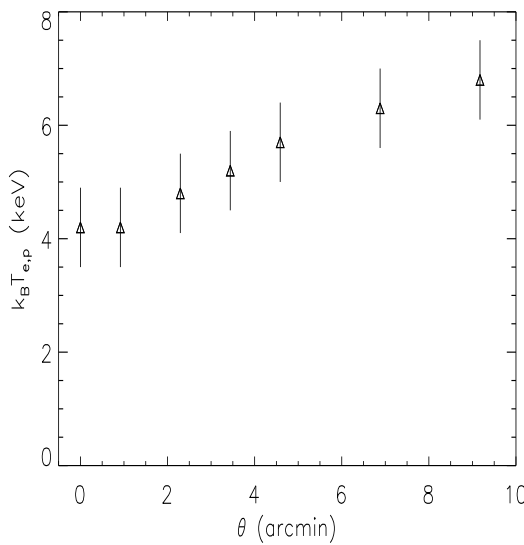


**Fig. 17.** The radial profile of the projected temperature, as derived from the fit to the SZE spectra in Perseus in the frequency range 300–440 GHz with uncertainties of 1% (see Fig. 16), is shown as a function of the projected radius (in arcmin).

## 6.2. The Ophiuchus cluster

The Ophiuchus cluster is, at first approximation, an isothermal cluster with  $kT \sim 9.9$  keV (Watanabe et al. 2001). Moreover, being Ophiuchus a quite hot cluster, relativistic effects in the SZE spectrum are expected to be

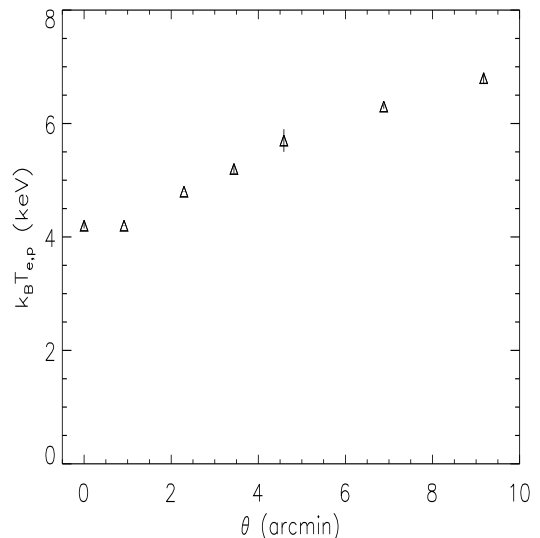
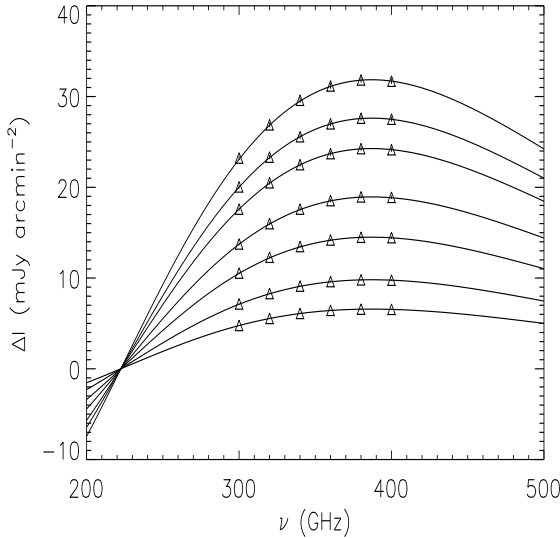


**Fig. 19.** As Fig. 17 but with uncertainties assumed at the level of 0.1% on the sampled SZE data points (see Fig. 16).

more prominent and this allows to obtain a better estimate of both the cluster temperature and density.

The SZE signal produced in Ophiuchus, calculated as described in Sect. 2, has been sampled at six frequencies between 300 and 400 GHz at seven different radii: 0, 35, 70, 120, 200, 300 and 500 kpc (see Fig. 20), assuming experimental uncertainties of 1%. The minimum radius at which

we sampled the radial profiles has been chosen taking into account that at the Ophiuchus distance ( $z = 0.028$ ), 1 arcmin corresponds to  $\sim 34$  kpc.



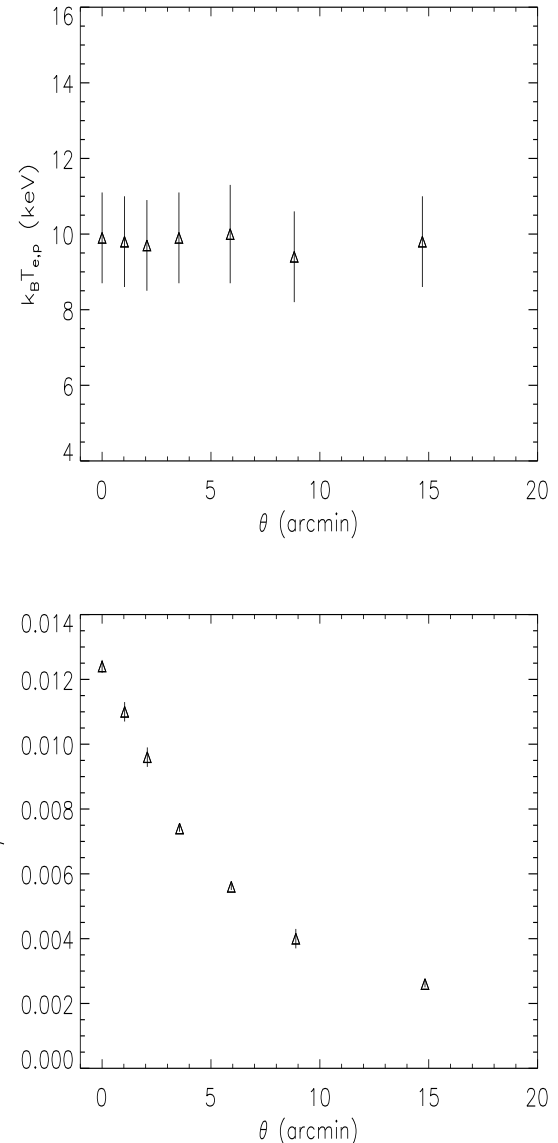
**Fig. 20.** The thermal SZE spectrum for the Ophiuchus cluster is shown at various projected radii of 0, 35, 70, 120, 200, 300 and 500 kpc (from top to bottom). The assumed uncertainties on the SZE data points is of 1%.

Fig. 21 shows the radial profiles of the projected temperature and optical depth obtained from the fit to SZE data. These results coherently indicate that the cluster temperature is constant with radius, within the errors, while the radial density profile can be derived from the optical depth radial profile by using the following model

$$n_e(r) = n_{e0} \left[ 1 + \left( \frac{r}{r_c} \right)^2 \right]^{-q_{th}}. \quad (34)$$

Therefore, we note that in a cluster with constant temperature profile, the deprojection procedure can be made by using only optical depth results without assuming any prior constraint taken from X-ray data. Hence, the thermal gas parameters derived from SZE and X-ray data can be directly compared.

The values derived from X-ray measurements are  $n_{e0} = 1.77 \times 10^{-2} \text{ cm}^{-3}$ ,  $r_c = 108 \text{ kpc}$  and  $q_{th} = 0.96$  (Johnston et al. 1981; Watanabe et al. 2001). The values we derive from the fit to the simulated SZE signals are  $n_{e0} = (1.7 \pm 0.2) \times 10^{-2} \text{ cm}^{-3}$ ,  $r_c = 118 \pm 2 \text{ kpc}$  and  $q_{th} = 1.00 \pm 0.07$ . The comparison between the best-fit profile to X-ray data and the one to the SZE data is shown in Fig. 22. We can see that the density profile derived from SZE measurements is very similar to that obtained from X-ray observations.



**Fig. 21.** The radial profile of the projected temperature (upper panel) and of the IC gas density (lower panel) as derived from the fit to the SZE spectra for Ophiuchus is shown as a function of the projected radius (in arcmin). We use SZE data points in the frequency range 300–400 GHz with uncertainties of 1% (see Fig. 20).

## 7. Discussion and conclusions

We derived in this paper a general formalism for describing the thermal SZE in galaxy clusters with a non-uniform temperature profile that can be applied to both cool-core clusters and non-cool core cluster with an isothermal or non-isothermal temperature structure.

In order to extract the temperature profile information from spatially resolved, spectroscopic SZE observations, we derive an inversion technique through which the electron distribution function can be extracted using a wide frequency range coverage of the SZE signal. We present

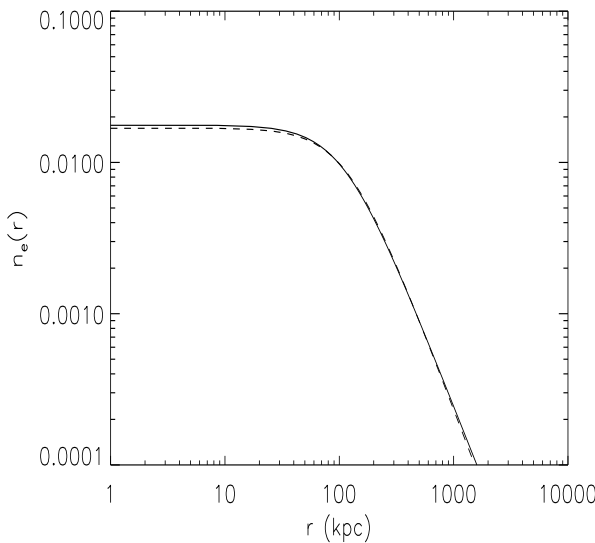


**Fig. 22.** The IC gas density profile of Ophiuchus as derived from X-ray observations (solid curve) is compared with the one derived from the optical depth radial profile shown in Fig.21 (dashed line) obtained from SZE simulated observations (see text for details).

extensive results of the fitting procedure used to extract the cluster temperature from a set of simulated spatially resolved spectroscopic SZE observations in different bands of the spectrum, from 100 to 450 GHz, and we discuss the optimal experimental and theoretical strategy.

The results of our analysis for three different cluster prototypes (A2199 with a low-temperature cool core, Perseus with a relatively high-temperature cool core, Ophiuchus with an isothermal temperature distribution) provide the required precision of the SZE observations and the optimal frequency bands for a determination of the cluster temperature similar or better than that obtainable from X-ray observations. The precision level of SZE-derived temperature is also discussed for the outer regions of clusters, an issue that is particularly relevant for accurate mass determination of galaxy clusters.

We also study the possibility to extract from our method the parameters characterizing the non-thermal SZE spectrum of the relativistic plasma contained in various astrophysical environments: the lobes of radio galaxies as well as the relativistic electrons co-spatially distributed with the thermal plasma in galaxy clusters with non-thermal phenomena (e.g. radio halos and/or hard X-ray excesses).

Based on our results, we conclude that the method we present here is the only method, so far, for SZE observations that is able to extract the crucial parameters of the cluster atmospheres (i.e. their temperature, density and additional non-thermal components) using only a single observational technique, i.e. spatially resolved spectroscopic SZE observations.

Other methods to extract the cluster temperature profile by using SZE observations have been presented (Holder & Loeb 2004), but they make use of a combination of the thermal SZE (which measures the electron pressure distribution) and of radio observations of the highly polarized scattered radiation coming from active galaxies associated to the cluster (which depends on the cluster electron density distribution). Holder & Loeb pointed out that current instruments should allow us to reach accuracy of the mass-weighted cluster temperature profiles of order of  $\sim 1$  keV, but under the assumption that the central radio source is steady over several million years. However, variable or beamed sources (like radio galaxies or jets/lobes of AGNs associated to the cluster) will leave observable signatures in the scattered emission. Therefore, this method could allow, in principle (e.g. with  $\mu$ K sensitivity observations to polarized emission), to measure the age of the central source by finding an edge to the polarized emission.

We noticed in this context, that combining this method with the independent temperature measurements from SZE spectral studies (that we discuss here) would allow to measure the time evolution of the central radio source.

In conclusion, our study shows that the next generation SZE experiments with spectroscopic capabilities, like those using FTS spectrometers with imaging capabilities (e.g. SAGACE, <http://oberon.roma1.infn.it/sagacemission/>, and/or MILLIMETRON), can provide precise temperature distribution over large radial distances for galaxy clusters even out to substantial redshift. This will allow to use SZE observations of clusters to better understand the physics of cluster atmospheres, to better reconstruct their total mass content and, eventually, to use clusters of galaxies as reliable astrophysical and cosmological probes.

*Acknowledgements.* We acknowledge stimulating discussions with P.de Bernardis and the SAGACE team.

## References

- Abramowitz, M. & Stegun, I. A., 1965, Handbook of Mathematical Functions with Formulas, Graphs and Mathematical Tables (Dover Book, N.Y.)
- Aghanim, N., Hansen, S.H. & Lagache, G., 2005, A&A, 439, 901
- Arnaud, M., 2005, arXiv:astro-ph/0508159
- Battistelli, E.S., De Petris, M., Lamagna, L. et al., 2003, ApJ, 598, L75
- Birkinshaw, M., 1999, PhR, 310, 97
- Boehm, C. & Lavalle, J., 2009, PhRvD, 79, 3505
- Borgani, S., Diaferio, A., Dolag, K. & Schindler, S., 2008, SSRv, 134, 269
- Churazov, E., Forman, W., Jones, C. & Böhringer, H., 2003, ApJ, 590, 225
- Colafrancesco, S., 2004, A&A, 422, L23
- Colafrancesco, S., 2005, A&A, 435, L9
- Colafrancesco, S. 2007, New Astron. Rev., 51, 394
- Colafrancesco, S., 2008a, ChJAS, 8, 61
- Colafrancesco, S., 2008b, MNRAS, 385, 2041

Colafrancesco, S. & Vittorio, N., 1994, ApJ, 422, 443  
 Colafrancesco, S., Mazzotta, P., Rephaeli, Y. & Vittorio, N., 1994, ApJ, 433, 454  
 Colafrancesco, S., Mazzotta, P. & Vittorio, N., 1997, ApJ, 488, 566  
 Colafrancesco, S., Marchegiani, P. & Palladino, E., 2003, A&A, 397, 27  
 Colafrancesco, S., Dar, A. & De Rújula, A., 2004, A&A, 413, 441  
 Colafrancesco, S., Marchegiani, P. & Perola, G.C., 2005, A&A, 443, 1  
 Colafrancesco, S. & Giordano, F., 2006, A&A, 454, L131  
 Colafrancesco, S. & Giordano, F., 2007, A&A, 466, 421  
 Colafrancesco, S. & Marchegiani, P., 2008, A&A, 484, 51  
 Colafrancesco, S. & Marchegiani, P., 2009, A&A in press, arXiv:0904.3429  
 Colafrancesco, S., Prokhorov, D. & Dogiel, V., 2009, A&A, 494, 1  
 De Petris, M., D'Alba, L., Lamagna, L. et al., 2002, ApJ, 574, L119  
 Dolgov, A.D., Hansen, S.H., Pastor, S. & Semikoz, D.V., 2001, ApJ, 554, 74  
 Ehlerlert, S. & Ulmer, M.P., 2009, arXiv:0906.2564  
 Enßlin, T.A. & Kaiser, C.R., 2000, A&A, 360, 417  
 Ettori, S. & Fabian, A.C., 1999, MNRAS, 305, 834  
 Ettori, S., Morandi, A., Tozzi, P., Balestra, I., Borgani, S., Rosati, P., Lovisari, L. & Terenziani, F., 2009, A&A, 501, 61  
 Fabian, A.C., Hu, E.M., Cowie, L.L. & Grindlay, J., 1981, ApJ, 248, 47  
 Fargion, D. & Salis, A., 1998, SvPhU, 41, 823  
 Finoguenov, A., Reiprich, T.H. & Böhringer, H., 2001, A&A, 368, 749  
 Guo, F. & Oh, S.P., 2008, MNRAS, 384, 251  
 Halverson, N.W., Lanting, T., Ade, P.A.R. et al., 2009, ApJ, 701, 42  
 Hansen, S.H., 2004, MNRAS, 351, L5  
 Holder, G.P. & Loeb, A., 2004, ApJ, 602, 659  
 Johnston, M. D., Bradt, H. V., Doxsey, R. E., Marshall, F. E., Schwartz, D. A. & Margon, B., 1981, ApJ, 245, 799  
 Johnstone, R.M., Allen, S.W., Fabian, A.C. & Sanders, J.S., 2002, MNRAS, 336, 299  
 Juin, J.B., Yvon, D., Réfrégier, A. & Yèche, C., 2007, A&A, 465, 57  
 Kang, H., Ryu, D., Cen, R. & Ostriker, J.P., 2007, ApJ, 669, 729  
 Knox, L., Holder, G.P. & Church, S.E., 2004, ApJ, 612, 96  
 LaRoque, S.J., Carlstrom, J.E., Reese, E.D. et al., arXiv:astro-ph/0204134  
 Lloyd-Davies, E.J., Ponman, T.J. & Cannon, D.B., 2000, MNRAS, 315, 689  
 Longair, M., 1993, High Energy Astrophysics, Cambridge University Press  
 Mohr, J.J., Reese, E.D., Ellingson, E., Lewis, A.D. & Evrard, A.E., 2000, ApJ, 544, 109  
 Nozawa, S. & Kohyama, Y., 2009, PhRvD, 79, 3005  
 Piffaretti, R., Jetzer, Ph., Kaastra, J.S. & Tamura, T., 2005, A&A, 433, 101  
 Pratt, G.W., Böhringer, H., Croston, J.H., Arnaud, M., Borgani, S., Finoguenov A. & Temple, R.F., 2007, A&A, 461, 71  
 Sato, K., Matsushita, K. & Gastaldello, F., 2009, PASJ, 61, S365  
 Staniszewski, Z., Ade, P.A.R., Aird, K.A. et al., 2009, ApJ, 701, 32  
 Sunyaev, R.A. & Zel'dovich, Ia.B., 1980, ARA&A, 18, 537  
 Verde, L., Kamionkowski, M., Mohr, J.J. & Benson, A.J., 2001, MNRAS, 321, L7  
 Voit G.M., 2000, ApJ, 543, 113  
 Watanabe, M., Yamashita, K., Furuzawa, A., Kunieda, H. & Tawara, Y., 2001, PASJ, 53 605  
 White, S.D.M., Navarro, J.F., Evrard, A.E. & Frenk, C.S., 1993, Nature, 366, 429  
 Wright, E.L., 1979, ApJ, 232, 348

## Appendix A: Comparing our results to the covariant formalism derivation of the SZE.

We compare here the SZE calculated according to the formalism of Wright (1979; W79) with the one calculated according to the derivation of Boehm & Lavalle (2009; BL09). For this last case, we refer to their eqs. (18)–(22), derived in the Thomson limit, that are therefore directly comparable with those derived by W79.

According to BL09, the correct expression of the SZE in the relativistic covariant formulation, is:

$$\Delta I_\gamma(E_k) = I_\gamma^{\text{in}}(E_k) - I_\gamma^{\text{out}}(E_k). \quad (\text{A.1})$$

The averages over the angles of the two contributions are given by the following expressions

$$\hat{I}_\gamma^{\text{out}}(E_k) = 2 \mathcal{K} \tau_{\text{nr}} I_\gamma^0(E_k), \quad (\text{A.2})$$

where  $\mathcal{K} \rightarrow 1$  in the Thomson limit, and

$$\begin{aligned} \hat{I}_\gamma^{\text{in}}(E_k) = & 2 \tau_{\text{nr}} \int dp \tilde{f}_e(E_p) \\ & \times \int d\mu' \int d\mu \frac{\mathcal{F}(\beta, \mu, \mu')}{\sigma_T} I_\gamma^0(tE_k). \end{aligned} \quad (\text{A.3})$$

Here, the function  $\tilde{f}_e(E_p)$  is normalized as to give  $\int d^3p/(2\pi)^3 \tilde{f}_e(E_p) = 1$ , where  $t = (1 - \beta\mu)/(1 - \beta\mu')$ , and the function  $\mathcal{F}$  is given by:

$$\begin{aligned} \mathcal{F}(\beta, \mu, \mu') \equiv & \frac{\beta^2 m^2}{(2\pi)^3} \frac{3\sigma_T}{16} \frac{(1 - \beta\mu')}{(1 - \beta\mu)^2} \\ & \times \left\{ 2 - 2K(1 - \mu\mu') + K^2 \left[ (1 - \mu\mu')^2 \right. \right. \\ & \left. \left. + \frac{1}{2}(1 - \mu^2)(1 - \mu'^2) \right] \right\}, \end{aligned} \quad (\text{A.4})$$

where  $K = [\gamma^2(1 - \beta\mu)(1 - \beta\mu')]^{-1}$ .

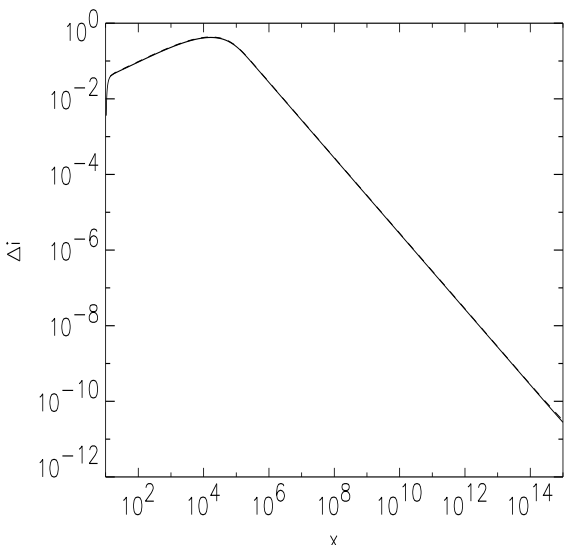
For the quantitative comparison of the two approaches, we have used the case of an electron population with a double power-law spectrum:

$$f_e(p) = A \begin{cases} p^{-s_1} & p_1 \leq p \leq p_{\text{break}} \\ p_{\text{break}}^{-s_1} (p/p_{\text{break}})^{-s_2} & p > p_{\text{break}} \end{cases} \quad (\text{A.5})$$

where  $p = \beta\gamma$ , that is normalized as to give  $\int_0^\infty f_e(p)dp = 1$ . We use parameters  $s_1 = 0.1$ ,  $s_2 = 3.0$ ,  $p_1 = 1$  e  $p_{\text{break}} = 100$ .

We notice that, with the use of the a-dimensional momentum  $p$  and the previous normalization, the expression for the function  $\mathcal{F}(\beta, \mu, \mu')$  in eq. (A.4) slightly changes: for consistency it must be multiplied by the factor  $(2\pi)^3/(\beta^2 m^2 \gamma^2)$ , as derived by using eqs. (16), (17) and (53) in BL09.

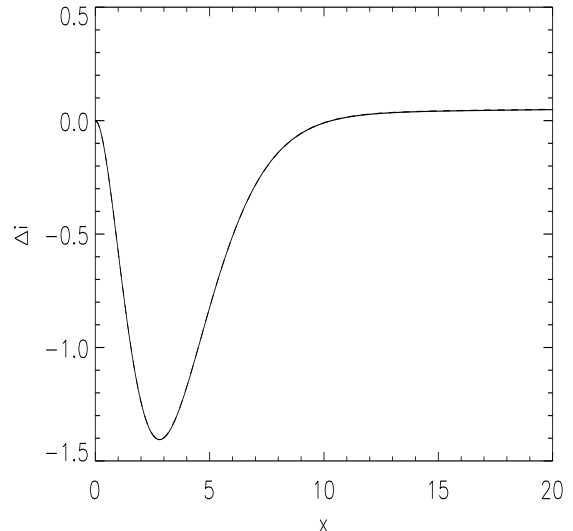
Fig. A.1 shows the SZE spectrum plotted over a wide frequency range,  $x = (h\nu)/(k_B T_0)$  from  $x = 10$  ( $\nu \sim 570$  GHz) up to  $x = 10^{15}$  ( $h\nu \sim 2.35 \times 10^2$  GeV) calculated up to first order for  $\tau = 1$  according to W79 (continuous curve) and that calculated according to BL09 (dashed line). As is clearly recognized, the two spectra are indistinguishable over the whole frequency range.



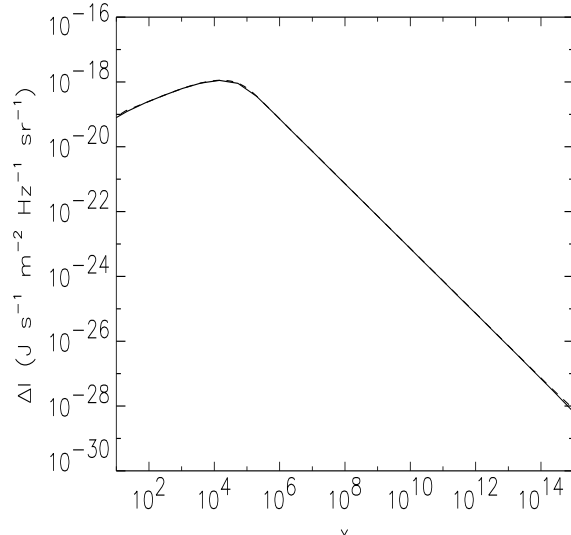
**Fig. A.1.** The SZE spectrum calculated following the method of W79 (solid line) and following the method of BL09 (dashed line). The horizontal axis shows the a-dimensional frequency  $x = (h\nu)/(k_B T_0)$  while the vertical axis shows the SZE brightness change  $\Delta i(x)$  in units of  $2(k_B T_0)^3/(hc)^2$ . No difference between the two approaches appears.

Fig. A.2 shows a blow-up of the SZE spectra in the microwave region ( $x = 0 - 20$ ). Also in this region we must conclude that the results obtained with the two formalisms are indistinguishable.

Fig. A.3 shows the comparison between the ICS emission (against the CMB photons) along the line of sight calculated in the approach of BL09 and in the standard approach (see e.g. Colafrancesco et al. 2005, see also Longair 1993) using also the Klein-Nishina cross-section, and assuming an electron spectrum as in eq.(A.5), with a density and spatial distribution such that  $\tau = 1$ . The two different calculations provide quite similar results, apart for the frequency range  $x > 10^{15}$ , at which the Klein-Nishina cross-section has a non-negligible effect (it decreases, in fact, the Compton scattering efficiency at high energies, see e.g. Fargion & Salis 1998).



**Fig. A.2.** Same as Fig. A.1 but with a zoom in the microwave frequency range at which the SZE telescope operate. Also in this low-frequency range, there is no difference between the two approaches.



**Fig. A.3.** The comparison of the ICS emission evaluated following the standard computational approach with the inclusion of the Klein-Nishina cross-section (solid line) and the one evaluated following the method of BL09 in the Thomson approximation (dashed line). No difference appears in the two approaches up to a frequency  $x \sim 10^{15}$ .

Based on the previous results, we can conclude that:  
i) for the SZE spectrum in the microwave-mm region the formalism of W79 can be used also in the case of relativistic electrons since it provides the same results of the covariant formalisms of BL09. In addition, the W79 formal-

ism, that uses a more simple expression requires a much shorter computing time w.r.t. the BL09 formalism.

ii) for the calculation of the ICS emission at high frequencies, the standard formalism is completely adequate since also in this case there is no difference w.r.t. the covariant formalism results. In addition, the standard formalism requires much shorter computing time and allows also the use of the Klein-Nishina cross-section effect without introducing additional complications in the numerical computation, as occurs - on the contrary - in eq.(46) of BL09.

Recently Nozawa & Kohyama (2009) analyzed the covariant formalism of the Sunyaev-Zeldovich effect for the thermal and nonthermal distributions and derived the frequency redistribution function identical to the W79 method assuming the smallness of the photon energy (in the Thomson limit). They also derive the redistribution function in the covariant formalism in the Thomson limit. These authors have shown that two redistribution functions are mathematically equivalent in the Thomson limit which is fully valid for the cosmic microwave background photon energies.

To summarize, the W79 and the covariant formalisms to calculate the SZE are fully equivalent, contrary to previous erroneous claims (see BL09), and the large advantage given by the standard calculations based on the W79 approach are due to the much shorter computing times.